Analytic Method for Radiometric Correction of Satellite Multispectral Scanner Data[1]

by

R.J. Woodham[2] and M.H. Gray[3]

Technical Report 87-1

January 1987

Laboratory for Computational Vision
Department of Computer Science
University of British Columbia
Vancouver, B.C., CANADA

[1] to appear in *IEEE Transactions on Geoscience and Remote Sensing*

[2] Fellow of the Canadian Institute for Advanced Research.

[3] Currently with the Surveys and Resource Mapping Branch, BC Ministry of Environment, Victoria, BC.

Abstract -- The problem of radiometric correction of multispectral scanner data is posed as the problem of determining an intrinsic reflectance factor characteristic of the surface material being imaged and invariant to topography, position of the sun, atmosphere and position of the viewer. A scene radiance equation for remote sensing is derived based on an idealized physical model of image formation. The scene radiance equation is more complex for rugged terrain than for flat terrain since it must model slope, aspect and elevation dependent effects. Scene radiance is determined by the bidirectional reflectance distribution function (BRDF) of the surface material and the distribution of light sources. The sun is treated as a collimated source and the sky is treated as a uniform hemispherical source. The atmosphere is treated as an optically thin, horizontally uniform layer. The limits of this approach are reviewed using results obtained with Landsat MSS images and a digital terrain model (DTM) of a test site near St. Mary Lake, British Columbia, Canada.

New results, based on regression analysis, are described for the St. Mary Lake site. Previous work is extended to take advantage of explicit forest cover data and to consider numeric models of sky radiance. The calculation of sky irradiance now takes occlusion by adjacent terrain into account. The results for St. Mary Lake suggest that the cosine of the incident solar angle and elevation are the two most important correction terms. Skylight and inter-reflection from adjacent terrain, however, also are significant.

Keywords -- Radiometric correction, topographic effect, atmospheric effect, digital terrain model (DTM), sky radiance, bidirectional reflectance distribution function (BRDF)

I. INTRODUCTION

Remote sensing benefits when data sets from different satellites, or different data sets from the same satellite, are directly comparable. Before direct comparison is possible, it is necessary to identify what it is that is to be compared. Ideally, the comparison would show changes in an intrinsic scene property and be invariant to other effects. But sensor measurements result from the interaction of several factors. Suppose the intrinsic property of interest is ground cover. The effects of surface material and topography must be separated from each other and from the effects of illumination, shadows, viewing direction and path phenomena.

The problem of radiometric correction of multispectral scanner date is here posed as the problem of determining an intrinsic reflectance factor characteristic of the surface material being imaged and invariant to topography, position of the sun, atmosphere and position of the viewer. A method for radiometric correction is described that uses an idealized physical model of image formation to disambiguate the effects of ground cover, topography, direct solar radiance, diffuse sky radiance and path radiance. If the parameters of the model are known or can be estimated, then a reflectance factor that is an intrinsic scene property related to ground cover can be computed.

It is by no means obvious that such a method is possible. Section II develops the required analytic tools. Particular attention is paid to delineating the fundamental limits of the approach. Section III applies the approach to remote sensing by including atmospheric effects. Necessary simplifying assumptions are described. Section IV presents results obtained with Landsat MSS images and a digital terrain model (DTM) of a test site near St. Mary Lake, British Columbia, Canada. Section V presents an extended discussion of the approach taken and the results obtained. Issues of methodology are emphasized. Conclusions are summarized in Section VI.

II. BACKGROUND AND METHODOLOGY

The amount of light reflected by a surface element in a given direction depends on its optical properties, on its microstructure and on the spatial and spectral configuration of the light sources. Intrinsic reflectance properties of a surface material are specified by the bidirectional reflectance distribution function (BRDF) introduced by Nicodemus *et al.* [1]. The BRDF is a complete specification of reflectance in that it allows one to determine how a surface will appear under any conditions of illumination and viewing. If the BRDF and the distribution of the light sources is given, a scene radiance equation can be derived. In this section, we consider the BRDF of a Lambertian reflector and of a class of reflectors first identified by Minnaert[2]. Scene radiance equations are presented both for collimated and for uniform hemispherical light sources. As a prerequisite, we consider coordinate systems for specifying the required directions. Finally, the question of measuring the reflectance properties of an arbitrary material is considered.

A. *Coordinate Systems*

In general, it is necessary to distinguish three different coordinate systems. The BRDF is specified in an object-centered coordinate system defined with respect to a plane tangent to the surface at a point of interest. Images are defined in a viewer-centered coordinate system. Digital terrain models, and other geocoded data, are specified in an earth-centered coordinate system. It is possible to define each of these coordinate systems independently and to develop full transformation equations from one to the other. For distant nadir-viewing sensors, the viewer-centered and earth-centered coordinate systems coincide, or at least can be made to coincide by geometric rectification.

To relate the incident and the reflected ray geometry, it is sufficient to develop transformation equations only for directions. There are several equivalent ways to define directions within a given coordinate system. The development here is based on spherical coordinates (θ,ϕ) shown in Fig. 1. The polar or zenith angle θ is measured from the Z-axis and the azimuth angle ϕ is measured counter-clockwise from the X-axis in the XY plane. (In navigation, the elevation angle is used instead of the zenith angle and azimuth is usually measured clockwise from the Y-axis, aligned with north, instead of counter-clockwise from the X-axis, aligned with east. These are the complements of the angles given here.)

First, consider a plane tangent to the surface at a point of interest. A local reference direction is chosen in the tangent plane and a Cartesian coordinate system is erected with the X-axis aligned with the reference direction and with the Z-axis aligned with the surface normal. Four angles (θ_i,ϕ_i) and (θ_r,ϕ_r) are required to specify an arbitrary incident and reflected ray geometry as shown in Fig. 2. Often, one considers materials whose reflectance properties are invariant with respect to rotations about the surface normal. This is equivalent to saying that only the difference in azimuth $(\phi_r - \phi_i)$ is required since the choice of a reference direction for the X-axis is arbitrary. For surfaces that are isotropic in this way, only three angles are required to specify the incident and the reflected ray geometry. Fig. 3 illustrates another way to specify these three angles. Clearly $i = \theta_i$ and $e = \theta_r$. Applying the cosine law for the sides of the spherical triangle formed by the incident ray, the reflected ray and the surface normal, one obtains

$$\cos(g) \;=\; \cos(\theta_i)\cos(\theta_r) + \sin(\theta_i)\sin(\theta_r)\cos(\phi_r - \phi_i) \tag{1}$$

(1) is used to determine the phase angle g from the corresponding $(\phi_r - \phi_i)$ and *vice versa.*

Now, consider an earth-centered coordinate system defined so that the X-axis points east, the Y-axis points north and the Z-axis points vertically upwards. (For a distant nadir-viewing sensor, the viewer-centered coordinate system coincides, provided the image X-axis is aligned with the west to east direction. For off-nadir viewing, the two coordinate systems differ and one must define additional transformations between the two.) A digital terrain model can be thought of as a function $z = f(x,y)$ defined in the earth-centered coordinate system. The direction of a surface normal can be found by taking the cross-product of any two vectors lying in the tangent plane, provided they are not parallel to each other. Two such vectors are $[1,0,p]$ and $[0,1,q]$ where $p = \partial f(x,y)/\partial x$ is the slope in the west to east direction and $q = \partial f(x,y)/\partial y$ is the slope in the south to north direction. The corresponding cross-product is $[-p,-q,1]$. The quantity (p,q) is called the gradient and is another way to specify direction in the earth-centered coordinate system.

A unit vector is obtained by dividing the vector $[-p,-q,1]$ by its magnitude. In spherical coordinates, a unit vector is given by $[\cos\phi\sin\theta, \sin\phi\sin\theta, \cos\theta]$. To find (p,q) from (θ,ϕ) one equates components of the corresponding unit vectors to obtain

$$\begin{aligned} p &= -\cos\phi\tan\theta \\ q &= -\sin\phi\tan\theta \end{aligned} \tag{2}$$

Conversely,

$$\begin{aligned} \phi &= \arctan(-q,-p) \\ \theta &= \arctan(\sqrt{p^2 + q^2}) \end{aligned} \tag{3}$$

The gradient (p,q) also has a simple geometric interpretation as the projection of the point (θ,ϕ) on the unit sphere from the center of the sphere to the plane tangent to the north pole, provided that the sign of the p and q axes is reversed from that of the x and y axes. This projection, called the gnomonic projection, has the advantage that coordinates p and q correspond directly to the first partial derivatives of surface elevation z. It has the disadvantage that p and q become unbounded as θ approaches $\pi/2$.

The gnomonic projection is one example of an azimuthal projection, so-called because latitude ϕ on the sphere becomes azimuth in the plane. Azimuthal projections, in general, are not area preserving. But, area deformation in an azimuthal projection is symmetric depending only on distance from the origin. By appropriate scale adjustment along the great circles of constant azimuth, it is possible to achieve a projection with the desired area preserving property. The result is called the azimuthal equal-area projection, denoted here by coordinates (s,t). Later, we use the azimuthal equal-area projection as the basis for a uniform tesselation of the sky hemisphere. The transformation from spherical coordinates (θ,ϕ) to rectangular coordinates (s,t) is given by,

$$\begin{aligned} s &= -\cos(\phi)\,\sin(\frac{\theta}{2}) \\ t &= -\sin(\phi)\,\sin(\frac{\theta}{2}) \end{aligned} \tag{4}$$

Conversely,

$$\begin{aligned} \phi &= \arctan(-t,-s) \\ \theta &= 2\,\arcsin(\sqrt{s^2+t^2}) \end{aligned} \tag{5}$$

This projection maps the hemisphere $0 \leq \theta \leq \pi/2$ onto the circle $s^2 + t^2 \leq 1/2$. It is area preserving in that, for any θ_0, $0 \leq \theta_0 \leq \pi/2$, the area of the circle $s^2 + t^2 \leq \sin^2(\theta_0/2)$ is proportional to the solid angle on the sphere $0 \leq \theta \leq \theta_0$.

Later, we also need to find i, e and g from the gradient (p,q). Let the light source direction have gradient (p_0,q_0). That is, the vector $[-p_0,-q_0,1]$ points in the direction of the light source. For nadir looking sensors, the vector [0,0,1] points in the direction of the viewer. Expressing the cosine of the angle between two vectors as a normalized dot product of the vectors, one obtains

$$\begin{aligned} \cos(i) &= \frac{1 + pp_0 + qq_0}{\sqrt{1+p^2+q^2}\,\sqrt{1+p_0^2+q_0^2}} \\ \cos(e) &= \frac{1}{\sqrt{1+p^2+q^2}} \\ \cos(g) &= \frac{1}{\sqrt{1+p_0^2+q_0^2}} \end{aligned} \tag{6}$$

B. *The Bidirectional Reflectance Distribution Function*

The intrinsic reflectance properties of a surface material are specified by the bidirectional reflectance distribution function (BRDF). The BRDF was introduced as a unified notation for the specification of reflectance in terms of both the incident and reflected ray geometry. The BRDF, denoted by the symbol f_r, is the ratio of the reflected radiance dL_r in the direction toward the viewer to the irradiance dE_i in the direction from a portion of the source. That is,

$$f_r(\theta_i,\phi_i;\theta_r,\phi_r) = \frac{dL_r(\theta_i,\phi_i;\theta_r,\phi_r;E_i)}{dE_i(\theta_i,\phi_i)} \qquad [\mathrm{sr}^{-1}] \tag{7}$$

Directions are given in spherical coordinates (θ,ϕ). Subscript i denotes quantities associated with the incident radiant flux and subscript r denotes quantities associated with the reflected radiant flux (see Fig. 1).

The BRDF is a function defined in terms of incident and reflected rays. It cannot be measured directly because any measurement situation inevitably involves incident and reflected beams (i.e., the light source and the viewer both subtend finite solid angles). This has important implications discussed below. First, however, suppose the BRDF is known analytically.

The BRDF allows one to determine scene radiance L_r for any given light source distribution and viewer geometry by integrating over the specified solid angles. A systematic approach to this problem has already been described[3]. Results for Lambertian surfaces and Minnaert surfaces are summarized below. (The derivations are in [3] and [4] respectively.)

An ideal (lossless) perfectly diffuse (Lambertian) surface has BRDF.

$$f_r = \frac{1}{\pi} \tag{8}$$

When there is some loss due to absorption, the BRDF of a Lambertian surface becomes

$$f_r = \frac{\rho}{\pi} \tag{9}$$

Where ρ is called the reflectance factor $(0 \le \rho \le 1)$.

When illuminated by a collimated source with irradiance E_0 measured perpendicular to the beam of light arriving from direction (θ_0, ϕ_0), one obtains

$$L_r = \frac{E_0}{\pi} \rho \cos(i) \tag{10}$$

When illuminated by a hemispherical uniform source with radiance L_0 over the visible hemisphere, one obtains

$$L_r = L_0 \rho \frac{1 + \cos(e)}{2} \tag{11}$$

Here, the dependence on e arises because differing surface elements see differing amounts of sky depending on surface slope. As slope increases, more of the sky is obscured. (Note, this is purely a local effect and does not take adjacent terrain into account.)

Minnaert[2] considered a class of surfaces that, under distant point source illumination, had brightness proportional to $\cos^k(i)\, f(e)$ where $f(e)$ denotes an arbitrary function of e. By applying Helmholtz reciprocity, Minnaert showed that $f(e) = \cos^{k-1}(e)$. Recasting Minnaert's derivation into the current notation, one obtains a class of ideal (lossless) surfaces with BRDF

$$f_r = \frac{k+1}{2\pi} [\cos\theta_i \cos\theta_r]^{k-1} \tag{12}$$

One could introduce a parameter ρ in (12) to account for some loss due to absorption, as was done in (9). This is not done here. The reflectance factor ρ is defined as the ratio of the radiant flux actually reflected by a sample surface to that which would be reflected into the same reflected-beam geometry by an ideal (lossless) Lambertian standard surface irradiated in exactly the same way as the sample. In any fixed imaging situation, the reflectance factor ρ, thus defined, is a scalar. By definition, ρ is invariant to conditions of illumination and viewing for Lambertian surfaces. For any other BRDF, however, the reflectance factor ρ, like the BRDF itself, is a function of (θ_i, ϕ_i) and (θ_r, ϕ_r). To emphasize its dependence on the incident and the reflected direction, ρ is called the bidirectional reflectance factor in [1].

When a surface with BRDF (12) is illuminated by a collimated source with irradiance E_0 measured perpendicular to the beam of light arriving from direction (θ_0,ϕ_0), one obtains

$$L_r = \frac{E_0\,(k+1)}{2\,\pi}\cos^k(i)\,\cos^{k-1}(e) \tag{13}$$

(This is equivalent to Minnaert's original result.)

An ideal (lossless) Lambertian surface corresponds to the case $k = 1$. For the case $k = 0$ the scene radiance equation is similar to that required for scanning electron microscope (SEM) images[5]. For the case $k = 1/2$ the scene radiance equation is constant for constant $\cos(i)/\cos(e)$. This is similar to the one estimated for the lunar surface[6,7], and for regions of Mars[8].

When illuminated by a hemispherical uniform source with radiance L_0 over the visible hemisphere, one obtains

$$L_r = L_0\cos^{k-1}(e)\left[1 - \frac{\sin^{k+1}(e)}{2\pi}\left[\frac{\Gamma(\frac{1}{2})\Gamma(\frac{k+2}{2})}{\Gamma(\frac{k+3}{2})}\;F(\tfrac{k+1}{2},\tfrac{1}{2};\tfrac{k+3}{2};\sin^2(e))\right]\right] \tag{14}$$

where $\Gamma(x)$ is the gamma function and $F(\alpha,\beta;\gamma;z)$ is the hypergeometric series defined by,

$$F(\alpha,\beta;\gamma;z) = 1 + \frac{\alpha\cdot\beta}{\gamma\cdot 1}z + \frac{\alpha(\alpha+1)\beta(\beta+1)}{\gamma(\gamma+1)\cdot 1\cdot 2}z^2 + \frac{\alpha(\alpha+1)(\alpha+2)\beta(\beta+1)(\beta+2)}{\gamma(\gamma+1)(\gamma+2)\cdot 1\cdot 2\cdot 3}z^3 + \cdots \tag{15}$$

Convergence of the hypergeometric series is guaranteed when $\alpha + \beta - \gamma < 0$ and $|z| \leq 1$. These conditions are satisfied for all k and $0 \leq e \leq \pi/2$. For $k = 1$, (14) reduces to the Lambertian case (11) with $\rho = 1$.

The difference between (10) and (11) is not due to a difference in surface material but to the difference in irradiance. In both cases, the BRDF is given by (9). Similarly, the difference between (13) and (14) is due only to the difference in irradiance. The corresponding BRDF is given by (12). If there exist materials with this phenomenologically derived BRDF, then the parameter k is related to an intrinsic property of that material. It does not, for example, account for differences in irradiance.

C. *Measuring Reflectance Properties*

For many surfaces, the fraction of the total irradiance reflected toward the viewer depends only on the surface orientation. Horn[9] introduced the idea of a reflectance map to determine scene radiance as a function of surface orientation. A reflectance map is a useful representation because it compiles the relevant information about surface material, light source distribution and viewer position into a single function. When the BRDF and light source distribution are known, the reflectance map can be derived analytically, using the ideas discussed above. Many examples are demonstrated in [10].

In a laboratory setting, a reflectance map can be measured directly using a goniometer mounted sample or indirectly from the image of a calibration object of known shape. This was demonstrated for metal castings[11]. More recently, a measured reflectance map was used in a machine vision system that allows a robot to pick mixed parts out of a bin[12,13]. A reflectance map measured using a calibration object is directly applicable to image analysis of objects of unknown shape, but made of the same material and illuminated and viewed under the same conditions. Unfortunately, it is difficult to use measurements acquired under one condition of illumination and viewing to predict the reflectance map for another condition of illumination and viewing. To do that requires knowledge of the BRDF and, as noted above, the BRDF itself is not directly measurable.

The BRDF, defined by (7), is a derivative with instantaneous values that can never be measured directly. Any real measurement involves incident and reflected beams and hence can yield only average values of f_r over the finite solid angles subtended by the light source and viewer. When the BRDF is a smooth function of (θ_i,ϕ_i) and (θ_r,ϕ_r), it can be assumed that local average values yield good estimates of the corresponding instantaneous values. But, any real measurement also involves light reflected from a surface element with finite area and hence can yield only average values of f_r over the area subtended by the instantaneous field of view (IFOV) of the sensor. Most natural surfaces are not spatially smooth. Consequently, average values over the IFOV of the sensor are highly dependent on the spatial scale and are difficult to relate to the underlying BRDF's and microstructure of the surface material.

To illustrate, consider reflection off water. In the visible portion of the spectrum, water behaves as a specular reflector. This fact is anecdotally documented in the perfect mirror-like reflections seen in photographs of calm, clear lakes. When wind creates surface roughness, this mirror-like behavior is no longer observed in the large. Instead, the observed pattern of reflections is more diffuse. This does not mean that water ceases to be a specular reflector. Analytically, the observed pattern is the temporal and spatial integral of specular reflection from infinitessimal wave facets having differing instantaneous orientations. The observed pattern of sunlight (and moonlight) glitter on a wind-ruffled sea has been used to deduce information about sea state[14]. Knowledge that water behaves as a specular reflector is used both to evaluate analytic models of ocean wave state and to make measurements of the parameters that determine sea roughness, such as wind speed and direction.

Reflectance spectroscopy, a tool of analytic chemistry, determines optical properties of materials from samples of known microstructure. Many materials cannot be analyzed by traditional spectroscopic methods. Some of these materials can be ground into fine powders of known particle size and shape. Analytic models are developed to relate measured reflectance factors of powders to the optical properties of the material of which they are composed[15].

Relating measured brightness to models of surface microstructure is a standard method of investigation in astronomy, especially as applied to the lunar surface. Many investigators have measured reflectance properties of the moon. The goal was to predict physical properties of the lunar soil. Investigators experimented with hundreds of terrestrial materials and surface microstructures in an attempt to replicate the photometric properties on the moon. These experiments led to correct predictions of the composition, particle size and porosity of the lunar soil. The conclusion was that the lunar surface is an assembly of closely packed, randomly pointed, deep tunnels of all sizes, superimposed and juxtaposed. The photometric properties of the moon are determined primarily by the shadows cast by surface detail and not by the reflection of light from surface material. Indeed, the lunar surface is uncommon in that the same material and structure would collapse under its own weight if it were replicated in the gravitational field on the earth. Some earth vegetation, however, can have similar photometric properties. Minnaert[6] and Hapke[7] provide excellent reviews of the study of the photometric properties of the moon. The surprising thing about the moon is not only that it has brightness constant for constant $\cos(i)/\cos(e)$ but that this relationship persists over a wide range of spatial scales.

These ideas have been increasingly applied to remote sensing, especially to model reflectance of vegetation canopies. Goel and his colleagues have published a series of five papers that are illustrative of work in this area. (See [16] for recent results and for references to the related work.) The primary goal is to invert the canopy reflectance model to determine agrophysical parameters, given measured reflectances. Agrophysical parameters include: leaf reflectance, leaf transmittance, leaf area index (LAI), leaf angle distribution (LAD), planting density and direction, biomass, as well as reflectances and transmittances of underlying structures such as stems and soil. A secondary goal is to predict how a given canopy will appear under different conditions of illumination and viewing.

Basic theoretical modeling also is increasingly supported by field measurement. Field measurement is difficult, compared to laboratory measurement, in part, because it is not possible to control the illumination and, in part, because it is difficult to match the scale of measurement in the field to the scale of measurement of the satellite images to which the model will be applied.

III. AN IMAGE IRRADIANCE EQUATION FOR REMOTE SENSING

The atmosphere and adjacent targets complicate the scene radiance equation for remote sensing in a number of ways as illustrated in Fig. 4 and as discussed below. A target, not in shadow, sees an attenuated direct solar beam with irradiance $E_0 T_d \cos(i)$ where E_0 is the solar irradiance at the top of the atmosphere, T_d is the downward transmission through the atmosphere and i is the angle of incidence at the target. Values of E_0 applicable to Landsat MSS and TM, derived from [17], are given in Table I.

A target, even when in shadow, receives diffuse sky irradiance. Skylight includes three components. First, there is radiation from the sun that is scattered by the atmosphere to the target, including both single and multiple scattering. Second, there is radiation reflected from adjacent terrain that is scattered by the atmosphere back to the target. Third, there is radiation reflected directly to the target from adjacent terrain. This third component is called inter-reflection. Inter-reflection is included as one of the effects modeled in [18]. In areas of low reflectance, the components of sky radiance due to adjacent terrain are small. But, they may become significant for areas of high reflectance or in rugged terrain. Let E_S denote the sky irradiance, integrated radiance over the hemisphere of the sky, incident on a plane surface.

The fraction of the total irradiance reflected in the direction of the sensor depends on the BRDF of the target. But, this reflected radiance is further attenuated by the atmosphere before it reaches the sensor. Let T_u be the upward transmission through the atmosphere.

Adjacent terrain adds one other complication. Due to atmospheric scattering, some radiation will reach the sensor that does not come directly from the target in view. This is termed the adjacency effect[19]. We let path radiance L_P denote only the radiant energy that reaches the sensor due to backscatter from the direct solar beam, again including both single and multiple scattering. Single scattering from the direct solar beam, called primary scattering, is the major component of path radiance in optically thin atmospheres. The adjacency effect is small in areas of low reflectance but may become significant as the reflectance of the ground increases[20]. As the reflectance of the ground increases, sky radiance also increases, especially near the horizon. Adjacent targets of high reflectance increase both upward radiance and downward sky radiance at the target. These two effects are difficult to separate, especially in areas of rugged terrain[21].

Extending results to atmospheres with significant multiple scattering requires a solution to the radiative transfer problem for the ambient radiation field[22]. This further couples all atmospheric effects together and makes it difficult to treat them separately.

A. *Simplifying Assumptions*

A full treatment of all components of the image irradiance equation is currently not feasible. Instead, five simplifying assumptions are made:

1. The atmosphere is assumed to be an optically thin, horizontally homogeneous layer. This reduces a three-dimensional problem to a one-dimensional problem by allowing optical depth to be defined as a function of elevation.

2. Radiation arising from adjacent targets, including clouds, is not considered.

3. The sensor views the target from directly overhead.

4. The sky is assumed to be a uniform hemispherical source with radiance varying as a function of elevation.

5. Ground cover is assumed to be Lambertian with BRDF $f_r = \frac{\rho}{\pi}$ where ρ is the intrinsic surface reflectance factor to be recovered.

Assumptions 1 and 2 are the most restrictive in that they allow radiometric correction to be defined as a local function of elevation and surface orientation. Relaxing 1 and 2 necessitates analysis over extended spatial contexts. Assumption 3 simplifies the coordinate transformations required but is otherwise not restrictive. The model can easily be extended to off-nadir sensors. Assumptions 4 and 5 are straightforward to relax if better models become available. An image irradiance equation can be derived for any distribution of sky radiance and for any given BRDF. But, as noted above, if the ground cover is not Lambertian, the reflectance factor ρ is no longer a scalar in that it cannot be defined invariant to conditions of illumination and viewing.

B. *Image Irradiance Equation*

With these assumptions, image irradiance $E(x,y)$, including atmospheric effects, becomes

$$E(x,y) = T_u \frac{\rho}{\pi} \left(E_0 \, T_d \cos(i) + E_S \frac{(1 + \cos(e))}{2} \right) + L_P \tag{16}$$

where i is the solar incident angle, e is the surface slope and ρ is the surface reflectance factor. It remains to find expressions for T_u, T_d, E_S and L_P as functions of elevation. The upward and downward transmissions are easily derived once optical thickness is introduced as an auxiliary quantity.

C. *Optical Thickness*

The optical thickness τ of an atmospheric mass measures the total extinction experienced by a light beam passing through it. (For the case of vertical transmission, τ is also called optical depth.) Optical thickness depends on the density and size distribution of particles in the atmosphere and on their scattering and absorption properties. For the visible and near infrared portion of the spectrum, three classes of particle are relevant: molecules, aerosols and ozone. Molecules of air are small with respect to the wavelength of light and contribute to Rayleigh scattering. Aerosols are particles large with respect to the wavelength of light and contribute to Mie scattering. Ozone absorbs radiation.

In previous work[23,4], the total optical thickness was assumed to vary exponentially with elevation. This may be a reasonable assumption under clear sky conditions when Mie scattering is minimized. Significant Mie scattering suggests a more complex dependence on elevation. For the exponential case, let

$$\tau(z) = \tau_0 \, e^{-z/H_\tau} \tag{17}$$

where parameter $\tau_0 = \tau(0)$ is the optical thickness at sea-level and parameter H_τ is the scale height. The upward and downward transmissions become

$$\begin{aligned} T_u(z) &= e^{-\tau(z)} \\ T_d(z) &= e^{-\tau(z)/\cos(g)} \end{aligned} \tag{18}$$

(When a sensor views a target from directly overhead, the phase angle g is identically the solar zenith angle.)

D. *Sky Irradiance and Path Radiance*

There have been a number of theoretical studies of radiative transfer mechanisms within the atmosphere that allow one to estimate sky radiance and path radiance. These studies assume a horizontally homogeneous atmosphere over a horizontal Lambertian surface. Results predict sky radiance and path radiance as a function of optical thickness and average background albedo. Since optical thickness depends on elevation, so do sky radiance and path radiance. One can assume that both sky irradiance and path radiance also vary almost exponentially with elevation. Let

$$E_S(z) = E_{S0}\, e^{-z/H_S} \tag{20}$$

$$L_P(z) = L_{P0}\, e^{-z/H_P} \tag{21}$$

where parameters $E_{S0} = E_S(0)$ and $L_{P0} = L_P(0)$ are the sky irradiance and path radiance at sea-level and parameters H_S and H_P are the respective scale heights.

Under the assumptions of this section, the image irradiance equation (16) is expressible in terms of six atmospheric parameters τ_0, H_τ, E_{S0}, H_S, L_{P0} and H_P. These are parameters that can be determined independently or estimated directly from remote sensing data. If these parameters are known, (16) can be solved for ρ to determine the intrinsic reflectance factor of the surface material.

IV. EXPERIMENTAL RESULTS

The study site is a 21.6 km by 30.4 km area surrounding St. Mary Lake in southeastern British Columbia, Canada (latitude N 49:36:30, longitude W 116:11:30). Elevation data along ridges and channels were manually digitized from the 1:50,000 Canadian National Topographic System (NTS) map sheet 82 F/9 (St. Mary Lake). The ridge and channel structure was represented initially using a Triangulated Irregular Network (TIN)[24]. Several grid representations were produced from the TIN. A 60 m grid DTM is used for the geometric rectification of Landsat images. Rectification is performed automatically using the method described in [25]. A 120 m grid was used in previous work on radiometric correction[4,26]. A 100 m grid is used in the current work, described below. Grid coordinates in the DTM correspond to the Universal Transverse Mercator(UTM) map projection used in Canadian NTS maps. The area has rugged terrain with elevations varying from 944 m to 2684 m above sea-level.

The exact timing of overflight for each Landsat MSS image is given in the ancillary data recorded with each scan line. The position of the sun is determined by a computer program based on the method of Horn[27] and verified using other public domain ephemeris software. The direction to the sun is represented as a gradient (p_0,q_0). The test site is small enough in area that (p_0,q_0) can be considered constant throughout.

Estimating the gradient (p,q) at each point in the DTM requires numerical differentiation. The computation can be unstable, especially if the number of quantization levels for elevation in the DTM is limited. In this work, the DTM's generated from the TIN used a cubic spline interpolant. With continuity of the gradient forced, a simple numerical estimate suffices. The gradient (p,q) is estimated by

$$p = \frac{f(x+1,y) - f(x-1,y)}{2\Delta x} \qquad q = \frac{f(x,y+1) - f(x,y-1)}{2\Delta y} \tag{22}$$

where Δx and Δy are the DTM grid spacings expressed in the same units as $f(x,y)$. The gradient is used to determine values for $\cos(i)$ and $\cos(e)$, as required, using (6). The gradient is also used to generate an ancillary mask file identifying terrain points that are flat. This mask file is available to exclude flat terrain when estimating parameters related to slope and aspect.

Another mask file is generated to identify terrain points that lie in shadow. A coordinate system is erected corresponding to a viewer looking from the direction of the sun and a hidden-surface algorithm is applied to determine terrain points that are visible from that viewpoint[26]. Points that are not visible are set in the shadow mask.

A. *Previous Work*

Topographic effects dominate Landsat images in areas of rugged terrain. This led to the development of automatic methods for geometric rectification. These methods use a DTM and the known position of the sun to predict image features that can be reliably and accurately located[28,25]. Once the image is rectified, the next step was to try to remove variations in brightness due to topography in order to better delineate changes due to ground cover. Experimental work consistently demonstrated, in addition to the topographic effect, a dependence of brightness on elevation[26,23]. The minimum recorded brightness is a decreasing function of elevation. The decrease is especially noticeable in the shorter wavelength bands. New methods to estimate path radiance L_P were based on this observation[23,4].

Sky radiance also was significant. In [26], it was noted that bright targets (eg., snow) in shadow were often brighter than dark targets (eg., conifer forest) in direct sunlight. A subsequent attempt to measure sky irradiance used cast shadow boundaries to estimate the required parameters[4]. Shadow boundaries were traversed in the direction from the sun azimuth. Shadow boundary points corresponding to transitions from light to dark typically correspond to terrain breaks and were not used. Points on cast shadow boundaries corresponding to transitions from dark to light vary with the position of the sun. One can therefore assume that the ground cover across a cast shadow boundary remains locally constant, provided that one excludes cast shadow points that happen also to coincide with terrain breaks. Further, one can assume that sky irradiance and optical thickness also are locally constant across cast shadow boundaries. Estimates are then easily obtained for τ_0 , H_τ , E_{S0} and H_S.

Results, based on cast shadow boundaries, were not entirely successful. Possible explanations include: hysteresis within the Landsat MSS itself, smoothing caused by geometric rectification and the atmospheric adjacency effect, mentioned above. More fundamentally, points near cast shadow boundaries are poor candidates for use in estimating overall sky irradiance because they correspond to points for which a significant fraction of the sky is occluded by adjacent terrain.

Some success was achieved using snow as a target of known reflectance[4]. This was demonstrated using a very low sun angle (elevation 13.8°) January 8, 1979, Landsat MSS image of St. Mary Lake with 43% of the study site in shadow. The acquisition of machine readable forest cover data from the B.C. Ministry of Forests provided a new opportunity for experimentation, as reported below.

B. *Target Selection*

A 25.0 km by 21.0 km sub-area is covered by nine B.C. Ministry of Forests 1:20,000 map sheets (82F.058, 059, 060, 068, 070, 078, 079 and 080). Machine readable versions of these maps were obtained. The maps are used to examine forest cover classes according to species composition, age, height, and % crown closure. About 70% of the total area is forest. The major forest species, in order of abundance, are: lodgepole pine (*Pinus contorta*), balsam fir (*Abies lasiocarpa*), englemann spruce (*Picea englemannii*), western larch (*Larix occidentalis*), and douglas-fir (*Pseudotsuga menziesii*). One quarter of the forested area is non-commercial alpine forest. Many of the accessible, merchantable stands have been harvested. (Recent harvesting accounts for over 10% of the forested area.) The remaining 30% of the total consists of: alpine areas (rock, snow, meadow) 15%; sub-alpine rock bluffs 7%; lakes and rivers 5%; roads, power-line right-of-ways and hayfields 3%.

The forest cover map data was used to examine areas of homogeneous ground cover. To test the model, we looked for forest types that occurred over a wide range of elevation, slope and aspect. For homogeneity, we also looked for uniform age and height and, preferably, a closed canopy. Unfortunately, very few natural vegetation types occur over a wide range of topographic positions. After much search, a target forest type was selected with the following attributes: Lodgepole pine ($\geq$ 80% pure); 80-100 years old; 10-20 m high; and 60-100% crown closure. Over the study site, the target set had the following range of topographic attributes: elevation 1205-2102 m; incident solar angle i 21.7-78.0 degrees; and slope angle e 7.2-35.7 degrees.

A mask file was generated for all Landsat MSS image pixels lying entirely within the polygonal map regions defining the target set. This mask file was manually edited to remove pixels corresponding to roads, landings and small bare patches that were visible on 1:12,000 aerial photographs but that were not included in the forest cover maps. The final target set consisted of 329 pixels. The topographic distribution of the target set is shown in Fig. 5.

Before proceeding to describe the analysis of the target set, we discuss briefly how models of sky radiance can be implemented to take into account portions of the sky that are obscured by adjacent terrain.

C. *Sky Radiance, Including Adjacent Terrain*

In order to implement numerical models of sky radiance, it is useful to divide the sky hemisphere into discrete cells. One can then associate a point source with each cell weighted according to sky radiance integrated over the solid angle subtended by that cell. As described above, a synthetic image is generated and summed with those from all other point source locations. Because shadow calculation is included from each point source direction, the final sum excludes, at each point, directions obscured from the sky by adjacent terrain.

To facilitate experimentation with a variety of sky radiance distributions, one seeks a tessellation of the sky hemisphere such that: each cell has the same area (i.e., subtends the same solid angle); each cell has the same, approximately round, shape; and the number of cells is large enough to provide sufficient numerical accuracy. Suitable tessellations of the sky hemisphere can be achieved by any regular tessellation of the circle $s^2 + t^2 = 1/\sqrt{2}$ in the azimuthal equal-area projection. Here, we use a uniform hexagonal tessellation of the (s,t) plane and defined a point source location at the center of each cell. The grid spacing chosen resulted in a uniform tessellation of the hemisphere into 109 point source locations, each point source corresponding to an equal solid angle of sky.

D. *Regression Analysis*

Multiple linear regression is one analysis tool that can be applied to the image irradiance equation (16). Of course, the model equation itself is not linear so that some reformulation is required. One idea is to treat elevation separately by stratifying the target set into subsets each with a narrow elevation range. For each subset, elevation is treated as constant. Coefficients determined by regression analysis of each subset could then be used to estimate the dependence of the path radiance, sky radiance and atmospheric transmission terms on elevation. Unfortunately for our test site and target set, there were not enough data points over a sufficient range of the independent variables to yield statistically significant results for each subset.

A second idea is to linearize the model equation directly. If the terms T_u, T_d, E_S and L_P each are approximated by a function of the form $a\, z + b$ then the resulting model equation is linear in the eight terms $\cos(i)$, $\cos(e)$, z, $z \cos(i)$, $z \cos(e)$, z^2, $z^2 \cos(i)$ and $z^2 \cos(e)$. Regression analysis for the target set showed that not all eight terms were correlated, at the 99% significance level, to measured brightness. Various subsets of the eight terms were then considered before settling on a model involving the four variables, $\cos(i)$, $\frac{1+\cos(e)}{2}$, z and z^2. The reason for expressing the $\cos(e)$ term in this way is to retain the connection to (11). Regression involving these four variables corresponds to a model in which target radiance depends on the cosine of the solar incident angle, the cosine of the slope and elevation (true of (16)), but with no coupling between them (not true of (16)).

As expected from previous work, the cosine of the solar incident angle is the most important variable for all bands, followed by elevation z. The third most important term was the cosine of the slope. Unexpected to us, however, the correlation with $\cos(e)$ was consistently negative, once corrections for $\cos(i)$ and z had been applied. One possible explanation for this negative correlation is that it arises as an artifact of the correction applied for $\cos(i)$. (This could happen, for example, if the correlation with $\cos(i)$ were high but the relationship was non-linear.) The way to rule this out would be to repeat the analysis using targets of constant $\cos(i)$. Again, unfortunately, there were not enough data points of constant $\cos(i)$ to yield a statistically significant conclusion, one way or the other.

Another possibility is that treating skylight as a uniform hemispherical source is unrealistic. To rule this out, the analysis was repeated using other models of skylight[29], including one measured empirically by colleagues in Geography[30]. The negative correlation with skylight persisted in all cases. One side effect of our method to implement empirical models of skylight is that shadow calculation allows adjacent terrain to be taken into account. Obscuration of the sky by adjacent terrain means that the amount of sky seen at each surface element is not a local function of the slope e, as is the case in (11). Negative correlation with skylight can, in fact, be interpreted as positive correlation with adjacent terrain.

Synthetic images are shown in Fig. 6. The synthetic image of a hemispherical uniform sky model, including shadowing by adjacent terrain, is shown in Fig. 6(c) and can be compared visually to Fig. 6(b). Observe that, for a given slope and aspect, brightness in Fig. 6(c) decreases with descent from a ridge into its valley.

Let this numerical model define a new variable called *topo*. In the absence of specific measurements of sky radiance for the location, date and time of image acquisition, *topo* provides a useful estimate of sky radiance under clear sky conditions. Indeed, when regression analysis was repeated considering *topo* and other sky models as regression variables in place of $\frac{1+\cos(e)}{2}$, the model using *topo* produced a slightly higher coefficient of determination and a slightly lower standard error in all cases and for all bands. Using $\cos(i)$, *topo*, z and z^2 as regression variables, the equations derived for each band of a September 15, 1981, Landsat MSS image are

$$
\begin{aligned}
E_4(x,y) &= 0.541 + 0.0781 \cos(i) - 3.79\times10^{-4}\, z + 1.10\times10^{-7}\, z^2 - 0.0185\, \boldsymbol{topo} \\
&\qquad (R^2 = 0.46 \quad SE = 0.014) \\
E_5(x,y) &= 0.350 + 0.0903 \cos(i) - 2.76\times10^{-4}\, z + 0.86\times10^{-7}\, z^2 - 0.0193\, \boldsymbol{topo} \\
&\qquad (R^2 = 0.60 \quad SE = 0.012) \\
E_6(x,y) &= 0.856 + 0.239 \cos(i) - 7.79\times10^{-4}\, z + 2.18\times10^{-7}\, z^2 - 0.0456\, \boldsymbol{topo} \\
&\qquad (R^2 = 0.71 \quad SE = 0.024) \\
E_7(x,y) &= 2.25 + 0.693 \cos(i) - 21.0\times10^{-4}\, z + 5.71\times10^{-7}\, z^2 - 0.139\, \boldsymbol{topo} \\
&\qquad (R^2 = 0.74 \quad SE = 0.065)
\end{aligned}
\tag{23}
$$

where $E_i(x,y)$ is in $\mathrm{mW\cdot cm^{-2}\cdot sr^{-1}}$, $(i = 4,5,6,7)$, z is in meters and $\cos(i)$ and ***topo*** are unitless. R^2 is the coefficient of determination (i.e., the fraction of the total variance accounted for by regression) and SE is the standard error, also in $\mathrm{mW\cdot cm^{-2}\cdot sr^{-1}}$. A corrected image is obtained by using the regression equations (23) to remove the variance predicted by the model variables. The original false color infrared image and the corrected image are shown in Fig. 7.

Correlation coefficients for the regression analysis are given in Table II. Examination of regression residuals as a function of the independent variables indicated no discernible trends. This can be confirmed by the near zero correlation between the bands of the corrected image and the independent variables for the target set (columns (b)). There is, however, some residual correlation when all points are considered (columns (a)).

Table III gives the correlation between the regression variables, both for the target set and for all points. High correlation between regression variables can cause the analysis to be unstable. There is almost no correlation between $\cos(i)$ and the other three variables when all points are considered. (For the target set, correlations are higher.) Significant correlation exists between $\cos(e)$ and z since the more rugged terrain tends to occur at higher elevations. Of course, $\cos(e)$ and *topo* are highly correlated, especially for the target set, and there is little to choose between them.

V. DISCUSSION

A. *Geometric Considerations*

For nadir viewing sensors, such as Landsat, geometric and radiometric correction are considered separately. This works well because negligible radiometric error is introduced by geometric preprocessing that, in effect, presumes all targets are seen from the vertical and through the same atmosphere. Thus, radiometric correction, as described here, can be applied after the image has been geometrically rectified.

Independence cannot be presumed for off-nadir sensors, such as SPOT. Algorithms for radiometric correction require the local incident and reflected beam geometry at the time of target acquisition. This is certainly required to correct for differing atmospheric paths. To the extent that natural surfaces are not Lambertian, this is also required to adjust for the change in (θ_r,ϕ_r) from actual to rectified sensor position.

For terrain of a given roughness, the maximum angle θ_r that occurs during imaging increases as the sensor becomes increasingly off-nadir. Thus, any dependence of the BRDF of the surface on θ_r becomes increasingly important to include in radiometric correction. This local information is lost if radiometric correction occurs only after geometric rectification.

B. *Spectral Considerations*

The BRDF also depends on the wavelength λ of the radiation in question. To make this dependence explicit, let $f_r(\theta_i,\phi_i;\theta_r,\phi_r;\lambda)$ be the spectral bidirectional reflectance distribution function (SBRDF). Selective reflection can alter the spectral distribution of the reflected beam. If there is interaction between spectral and geometric factors, as can be the case for materials with significant internal scattering, then the geometric distribution also is affected. On the other hand, if there is no interaction between wavelength and the geometric dependence of reflection then

$$f_r(\theta_i,\phi_i;\theta_r,\phi_r;\lambda) = f_r(\theta_i,\phi_i;\theta_r,\phi_r)\ f_r(\lambda) \tag{24}$$

where $f_r(\lambda)$ is a weighting function that determines relative reflection as a function of λ. If equation (24) holds, the SBRDF is said to be separable.

Unfortunately, there is little data to establish the extent to which there is interaction between geometric factors and spectral factors in remote sensing applications. There is some evidence that open forest cover, for example, is not separable in that there may be a differing amount of green (canopy) versus brown (bare soil) seen per pixel as the viewer moves from directly overhead to a more oblique position. Some canopy reflectance models assign different spectral characteristics to each constituent component to account for this phenomenon[31]. One can further examine the consequences of having a material whose SBRDF is not separable.

Suppose that a material is not separable in the sense of (24). Then there is a change in the spectral distribution of scene radiance as a function of the incident direction and the viewing direction. Consider again a Minnaert surface. The SBRDF of a Minnaert surface is not separable when k depends on λ. Remote sensing practitioners have investigated the hypothesis that k depends on λ[32-34]. Some have even suggested that this may be a way to accommodate atmospheric effects[8]. Estimates for k from three St. Mary Lakes Landsat MSS images acquired at a similar time of year are given in Table IV.

Now consider the two possible viewing situations shown in Fig. 8. Suppose that red, green and blue bands are obtained corresponding to the (known) values of $k = 1.0$, 0.5, and 0.25 respectively. Suppose $\theta = \pi/8$ corresponding to a solar zenith angle of $\pi/4$. The normalized components of red, green and blue are (0.539, 0.584, 0.607) for Fig. 8(a) and (0.341, 0574, 0.744) for Fig. 8(b). This represents a significant shift toward the blue for a rotation of only $\pi/4$ (45 degrees) about the point of observation. (Fig. 9 shows values of scene radiance and normalized red, green, blue for the full range of surface orientations in the plane of the incident and reflected beam.)

Suppose the above color values were obtained from remote sensing measurements of an unknown surface. There are at least two possible explanations. One explanation is that the surface is indeed of the Minnaert class with values of k that depend on λ. Some materials do change color with simple movement as nonseparability requires. (One example is the neck feathers of certain waterfowl that change colour with movement due to the presence of significant internal scattering by wax particles.) Another explanation is that there are additional components of scene irradiance in remote sensing to be considered. The above example only considers direct point source illumination. Any diffuse background irradiance adds complication, especially as in the case of skylight, if the spectral distribution of the background irradiance differs from that of the direct beam. A more plausible, indeed expected, explanation for this shift towards the blue when moving from a target facing the sun to a target facing away from the sun is that there is a corresponding shift towards the blue in irradiance as skylight begins to dominate direct sunlight.

C. *Atmospheric Considerations*

The six parameters introduced to model the atmosphere are tightly coupled together and difficult to treat independently. Without extended targets of near zero reflectance, it is difficult to separate path radiance from sky irradiance. Without extended shadow regions over the full range of elevations, it is difficult to estimate the dependence of sky irradiance and optical thickness on elevation. Without better models of the local dependence of sky irradiance on surface slope and adjacent terrain, it is difficult to separate optical thickness from sky irradiance.

The spatial distribution of sky radiance is not strictly uniform, even under clear sky conditions[29,35]. Partly cloudy conditions produce even more complex distributions. Measurements of sky radiance typically show brightening near the horizon indicating that adjacent terrain is important.

D. *Evaluation*

One evaluation criterion is purely subjective. It is possible to look both at synthetic images and at the corresponding corrected images to get a strong sense of the adequacy and range of the model being tested. One looks at corrected images to see if shadows are removed, if known homogeneous areas appear homogeneous independent of slope and aspect and if atmospheric corrections are appropriate over the full range of elevations that occur in the scene. Local anomalies in methods that otherwise have good global performance become readily apparent. The software and hardware tools to generate images in this way have been invaluable to our work. The ability to incorporate *a priori* knowledge of the scene domain as a synthetic image provides an appropriate representation for direct comparison to real images, both for geometric rectification and for subsequent interpretation.

Comparison of Fig. 7(a) and 7(b) reveals that the most evident change is the equalization of appearance for forest cover on all terrain aspects. (Some small topographic features have not been corrected. This can be seen, for example, along ridges and is likely due to smoothing of surface detail in the DTM.) The target set used in the regression is relatively dark, compared to non forest cover classes. Some evidence of dependence on aspect is still visible in alpine areas, which, by comparison, are relatively bright.

Of course, formal evaluation criteria need to be developed. The only obvious criterion is that the reflectance factor must lie between zero and one. The methods described generally achieve this except along seams of slight shadow miss-registration or along sharp ridges that have been smoothed in the DTM. Another possible criterion would be consistency in the estimated reflectance factor over time. Unfortunately, reflectance depends on many factors, including some like surface moisture that vary rapidly over the time period between successive Landsat overflights. It would be useful to test these methods on images acquired at different times on the same day.

To the extent that empirical measurements of scene radiance in one spectral band can be used to deduce physical characteristics of the scene, then these physical characteristics constrain the interpretation of scene radiance in other spectral bands. For example, in our view, multispectral scanner data in the near infrared provides the best estimate of intrinsic reflectance properties of surface material since atmospheric effects are minimized. These estimates of intrinsic surface properties can help to estimate atmospheric effects in other spectral bands, provided the overall spectral reflectance function is separable.

Of practical concern is the question of whether these methods improve the results obtained by image classification. A simple classification was performed, the details of which are reported in [36]. A nearest centroid classifier was used based on four ground cover classes: forest, clearcut, water and alpine. A truth map was constructed from the forest cover map. The classification of the uncorrected Landsat MSS image resulted in a map accuracy of 51% for forest cover. Examination of the corresponding confusion matrix revealed deficiencies typical of remote sensing of forest cover in rugged terrain. That is, many forest slopes with southeast aspect were classified as clearcut and many forest slopes with northwest aspect were classified as water. The classification of the corrected Landsat MSS image resulted in a map accuracy of 80% for forest cover. Correction for $\cos(i)$ achieved the greatest increase in classification accuracy. Elevation correction, in addition, decreased the miss-classification of forest as water. Correction for *topo*, while statistically significant in the regression, had little effect on the final classification.

VI. CONCLUSIONS

Conclusions following from this investigation are:

- Surface orientation (i.e., slope and aspect) is the most significant factor in determining scene brightness in areas of rugged terrain.
- Atmospheric effects also are significant and vary locally with elevation, particularly in the shorter wavelength bands.
- Sky radiance must be dealt with explicitly. In areas of rugged terrain, adjacent terrain makes a small, but nevertheless significant, contribution.
- Changes in the spectral composition of sky radiance as a function of direction also must be considered. For many surfaces, the apparent inseparability of measured spectral reflectance is caused by the changing spectral composition of scene irradiance rather than by an intrinsic reflectance property of the material itself.
- Parameters determining image irradiance can be related to physical models. Idealized physical models correctly characterize simple worlds and can be elaborated as the need is demonstrated.
- The problem of determining an intrinsic reflectance factor characteristic of the surface material and invariant to topography, position of the sun, atmosphere and position of the viewer, is, in general, not well-defined. A Lambertian reflector is the only material for which the bihemispherical reflectance factor can be expressed as a scalar, independent of the light source, viewer and surface geometry.

ACKNOWLEDGMENTS

Tom Poiker of Simon Fraser University provided original software for the representation and manipulation of DTM's. Digitization of NTS mapsheet 82 F/9 was done by Jim Little. Many individuals contributed to the software used in this paper. The authors particularly acknowledge the contributions of Tim Lee and Marc Majka. Ross Rose of MacDonald Dettwiler and Associates converted the BC Ministry of Forests forest cover map data for our use. Tony Kozak provided useful comments on regression. May Vink assisted with the preparation of the manuscript.

This report describes research done at the Laboratory for Computational Vision of the University of British Columbia. Support for the Laboratory's remote sensing research is provided, in part, by the UBC Interdisciplinary Graduate Program in Remote Sensing, by the Natural Sciences and Engineering Research Council of Canada (NSERC) under grants A3390, A0383 and SMI-51, and by the Canadian Institute for Advanced Research. Acquisition of the Landsat data used in this study was funded by a grant from the BC Ministry of Forests. Malcolm Gray acknowledges support from the Donald S. McPhee Fellowship fund and the MacMillan Bloedel Fellowship in Forest Mensuration.

REFERENCES

[1] F.E. Nicodemus, J.C. Richmond, J.J. Hsia, I.W. Ginsburg & T. Limperis, "Geometrical considerations and nomenclature for reflectance", *NBS Monograph 160*, National Bureau of Standards, Washington, D.C., 1977.

[2] M. Minnaert, "The reciprocity principle in lunar photometry", *Astrophys. J.* (93)403-410, 1941.

[3] B.K.P. Horn & R.W. Sjoberg, "Calculating the reflectance map", *Applied Optics* (18)1770-1779, 1979.

[4] R.J. Woodham & T.K. Lee, "Photometric method for radiometric correction of multispectral scanner data", *Canadian Journal of Remote Sensing* (11)132-161, 1985.

[5] K. Ikeuchi & B.K.P. Horn, "Numerical shape from shading and occluding boundaries", *Artificial Intelligence* (17)141-184, 1981.

[6] M. Minnaert, "Photometry of the moon", in *The Solar System Vol. III: Planets and Satellites*, G.P. Kuiper & B.M. Middlehurst (eds.), pp. 213-248, Univ. Chicago Press, 1961.

[7] B. Hapke, "Optical properties of the lunar surface", in *Physics and Astronomy of the Moon (2nd edition)*, Z. Kopal (ed.) pp. 155-211, Academic Press, 1971.

[8] A.T. Young & S.A. Collins, "Photometric properties of the mariner cameras and of selected regions of mars", *J. of Geophysical Research* (76)432-437.

[9] B.K.P. Horn, "Understanding image intensities", *Artificial Intelligence* (8)201-231, 1977.

[10] B.K.P. Horn, "Hill-shading and the reflectance map", *Proc. IEEE* (69)14-47, 1981.

[11] R.J. Woodham, "Reflectance map techniques for analyzing surface defects in metal castings", AI-TR-457, Artificial Intelligence Laboratory, MIT, Cambridge, MA, 1978.

[12] B.K.P. Horn, & K. Ikeuchi, "The mechanical manipulation of randomly oriented parts", *Scientific American* 251(2)100-111, 1984.

[13] K. Ikeuchi, H.K. Nishihara, B.K.P. Horn, P. Sobalvarro, S. Nagata, "Determining grasp configurations using photometric stereo and the PRISM binocular stereo system", *Int. J. Robotics Research* 5(1)46-65, 1986.

[14] G.N. Plass, G.W. Kattawar & J.A. Guinn, Jr., "Isophotes of sunlight glitter on a wind-ruffled sea", *Applied Optics* (16)643-653, 1977.

[15] W.W. Wendlandt & H.G. Hecht, *Reflectance Spectroscopy*, John Wiley & Sons, New York, NY, 1966.

[16] N.S. Goel & D.W. Deering, "Evaluation of a canopy reflectance model for LAI estimation through its inversion", *IEEE Trans. Geoscience and Remote Sensing* (GE-23)674-684, 1985.

[17] M.P. Thekaekara, "Proposed standard values of the solar constant and solar spectrum" *Journal of Environmental Sciences* (13)6-9, 1970.

[18] D.S. Kimes & J.A. Kirchner, "Modeling the effects of various radiant transfers in mountainous terrain on sensor response" *IEEE Trans. Geoscience and Remote Sensing* (GE-19)100-108, 1981.

[19] J. Otterman & R.S. Fraser, "Adjacency effects on imaging by surface reflection and atmospheric scattering: cross radiance to zenith", *Applied Optics* (18)2852-2860, 1979.

[20] J. Otterman, S. Ungar, Y. Kaufman & M. Podolak, "Atmospheric effects on radiometric imaging from satellite under low optical thickness conditions", *Remote Sensing of Environment* (9)115-129, 1980.

[21] J. Dozier & J. Frew, "Atmospheric corrections to satellite radiometric data over rugged terrain", *Remote Sensing of Environment* (11)191-205, 1981.

[22] R.E. Turner & M.M. Spencer, "Atmospheric model for correction of spacecraft data", *Proc. 2nd Int. Symp. Remote Sensing of Environment*, pp. 895-934, 1972.

[23] R.W. Sjoberg,& B.K.P. Horn, "Atmospheric effects in satellite imaging of mountainous terrain", *Applied Optics* (22)1702-1716, 1983.

[24] T.K. Peucker, R.J. Fowler, J.J. Little & D.M. Mark, "The triangulated irregular network", *Proc. of the Digital Terrain Models Symp.*, American Society of Photogrammetry, pp. 516-532, St. Louis, May 9-11, 1978.

[25] J.J. Little, "Automatic registration of Landsat MSS images to digital elevation models", *Proc. IEEE Workshop on Computer Vision: Representation and Control*, Rindge, NH, pp. 178-184, 1982.

[26] R.J. Woodham, "Using digital terrain data to model image formation in remote sensing", *Proc. SPIE* (238)361-369, 1980.

[27] B.K.P. Horn, "The position of the sun", AI-WP-162, Artificial Intelligence Laboratory, MIT, Cambridge, MA, 1978.

[28] B.K.P. Horn & B.L. Bachman "Using synthetic images to register real images with surface models", *Comm. ACM* (21)914-924, 1978.

[29] M.D. Steven, "Standard distributions of clear sky radiance", *Quarterly Journal of the Royal Meteorological Society* (106)57-61, 1977.

[30] K.E. Stewart, "The angular distribution of diffuse solar radiation over the sky hemisphere", M.Sc. Thesis, Dept. of Geography, University of British Columbia, Vancouver, B.C, 1984.

[31] X. Li & A.H. Strahler, "Geometric-optical modeling of a conifer forest canopy" *IEEE Trans. Geoscience and Remote Sensing* (GE-23)705-721, 1985.

[32] J.A. Smith, T.L. Lin & K.J. Ranson, "The lambertian assumption and landsat data", *Photogrammetric Engineering and Remote Sensing* (46)1183-1189, 1980.

[33] C.O. Justice, S.W. Wharton & B.N. Holben, "Application of digital terrain data to quantify and reduce the topographic effect on landsat data", *International Journal of Remote Sensing* (2)213-230, 1981.

[34] P.M. Teillet, B. Guindon & D.G. Goodenough, "On the slope-aspect correction of multispectral scanner data", *Canadian Journal of Remote Sensing* (8)84-106, 1982.

[35] J.A. Kirchner, S. Youkhana & J.A. Smith, "Influence of sky radiance distribution on the ratio technique for estimating bidirectional reflectance", *Photogrammetric Engineering and Remote Sensing* (48)955-959, 1982.

[36] M.H. Gray, "Radiometric correction of satellite imagery for topographic and atmospheric effects", M.Sc. Thesis, Faculty of Forestry, University of British Columbia, Vancouver, B.C., 1986.

Solar Irradiance at the Top of the Atmosphere						
Landsat MSS:						
Band	4	5	6	7		
Wavelength Interval (μm)	.5 - .6	.6 - .7	.7 - .8	.8 - 1.1		
Percentage of Solar Constant	13.1	11.2	9.1	18.4		
Solar Irradiance[1] ($mW \cdot cm^{-2}$)	17.7	15.1	12.4	24.9		
Landsat TM:						
Band	1	2	3	4	5	7
Wavelength Interval (μm)	.45 - .52	.52 - .60	.63 - .69	.76 - .9	1.55 - 1.75	2.08 - 2.35
Percentage of Solar Constant	10.2	10.3	6.6	10.8	3.3	1.6
Solar Irradiance[1] ($mW \cdot cm^{-2}$)	13.9	13.9	8.9	14.6	4.5	2.1

[1] based on solar constant of 135.3 $mW \cdot cm^{-2}$. This value is considered accurate to ± 2.1 $mW \cdot cm^{-2}$ for a quiet sun at the mean sun-to-earth distance. It is estimated that the solar constant varies from 130.9 $mW \cdot cm^{-2}$ at aphelion to 139.9 $mW \cdot cm^{-2}$ at perihelion.

Table I. Values of solar irradiance for a quiet sun at the top of the atmosphere at the mean sun-to-earth distance, for Landsat satellites. TM band 6 (10.4 - 12.5 μm) is not included since there is negligible solar irradiance at the top of the atmosphere in this wavelength interval. The table is derived from standard ANSI/ASTM E 490 - 73a "Solar constant and air mass zero solar spectral irradiance tables", proposed by Thekaekara[17] and adopted in 1973, in slightly modified form, by ASTM Committee E-21 on Space Simulation and Applications of Space Technology. The value for each Landsat band is obtained by integrating the standard solar spectral irradiance curve over the specified wavelength interval.

Correlation coefficients								
	Landsat MSS Band (raw data)							
	4		5		6		7	
	(a)	(b)	(a)	(b)	(a)	(b)	(a)	(b)
cos(i)	0.512	0.559	0.508	0.731	0.715	0.742	0.713	0.732
elevation	0.193	-0.108	0.275	0.162	-0.103	-0.161	-0.187	-0.230
cos(e)	-0.073	0.291	-0.092	0.263	0.052	0.373	0.086	0.376
topo	0.021	0.211	0.038	0.271	0.044	0.277	0.043	0.254
	Landsat MSS Band (corrected for cos(i))							
	4		5		6		7	
	(a)	(b)	(a)	(b)	(a)	(b)	(a)	(b)
cos(i)	0.272	-0.086	0.249	-0.023	0.263	-0.134	0.230	-0.159
elevation	0.216	-0.282	0.308	0.017	-0.144	-0.494	-0.261	-0.595
cos(e)	-0.112	-0.046	-0.136	-0.176	-0.002	-0.085	0.042	-0.083
topo	-0.015	-0.131	0.002	-0.146	-0.031	-0.211	-0.037	-0.246
	Landsat MSS Band (corrected for cos(i) and elevation)							
	4		5		6		7	
	(a)	(b)	(a)	(b)	(a)	(b)	(a)	(b)
cos(i)	0.274	-0.088	0.262	-0.073	0.237	-0.108	0.203	-0.119
elevation	0.306	0.018	0.253	0.016	0.104	-0.012	0.096	-0.023
cos(e)	-0.203	-0.180	-0.167	-0.257	-0.165	-0.285	-0.149	-0.312
topo	-0.085	-0.196	-0.059	-0.240	-0.120	-0.283	-0.111	-0.320
	Landsat MSS Band (corrected for cos(i), elevation and topo)							
	4		5		6		7	
	(a)	(b)	(a)	(b)	(a)	(b)	(a)	(b)
cos(i)	0.281	0.019	0.268	0.046	0.249	0.035	0.216	0.051
elevation	0.310	0.044	0.257	0.043	0.110	0.030	0.102	0.027
cos(e)	-0.173	-0.013	-0.137	-0.061	-0.110	-0.049	-0.089	-0.046
topo	-0.040	0.008	-0.014	-0.003	-0.039	0.006	-0.023	0.006

Table II. Correlation coefficients during the regression analysis of the September 15, 1981, Landsat MSS image. Columns (a) are the overall correlation coefficients for all points, except those in shadow or on flat terrain. Columns (b) are the correlation coefficients restricted to the selected target points.

Correlation Between Regression Variables								
	cos(i)		elevation		cos(e)		topo	
	(a)	(b)	(a)	(b)	(a)	(b)	(a)	(b)
cos(i)	1.0	1.0	-0.011	0.206	0.113	0.515	0.134	0.501
elevation	-	-	1.0	1.0	-0.376	-0.154	0.016	0.139
cos(e)	-	-	-	-	1.0	1.0	0.685	0.819
topo	-	-	-	-	-	-	1.0	1.0

Table III. Correlation coefficients between the regression variables for the position of the sun corresponding to the September 15, 1981, Landsat MSS image. Columns (a) are the overall correlation coefficients for all points, except those in shadow. Columns (b) are the correlation coefficients restricted to the selected target points.

Estimates of the Minnaert coefficient k						
Date	Sun		k			
	el	az	band 4	band 5	band 6	band 7
25/Sep/74	35.2	149.2	0.22	0.47	0.77	1.05
17/Sep/79	37.8	146.6	0.27	0.55	0.78	0.99
15/Sep/81	38.0	145.1	0.23	0.35	0.58	0.86

Table IV. Estimates of the Minnaert coefficient k for each Landsat MSS band from images acquired over St. Mary Lake on three different dates. All points are considered, except those lying in shadow or on flat terrain.

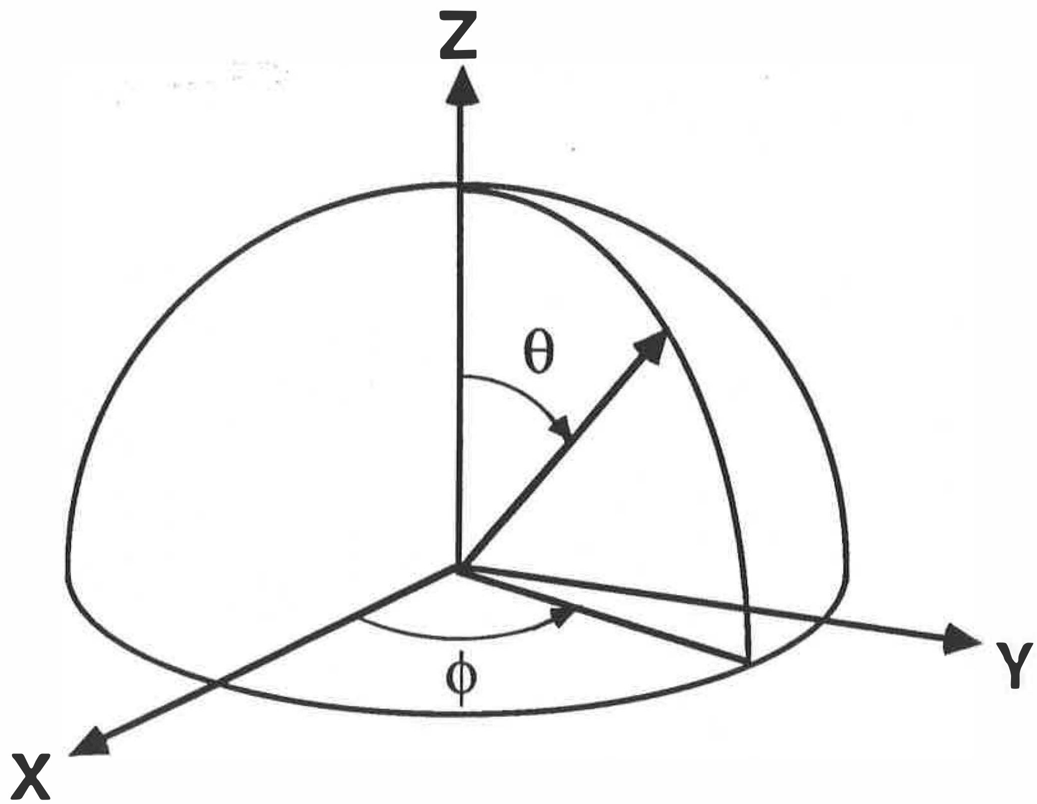

Fig. 1 Directions can be represented by points on the unit sphere. The polar or zenith angle θ is measured from the Z-axis and the azimuth angle ϕ is measured counter-clockwise from the X-axis in the XY plane.

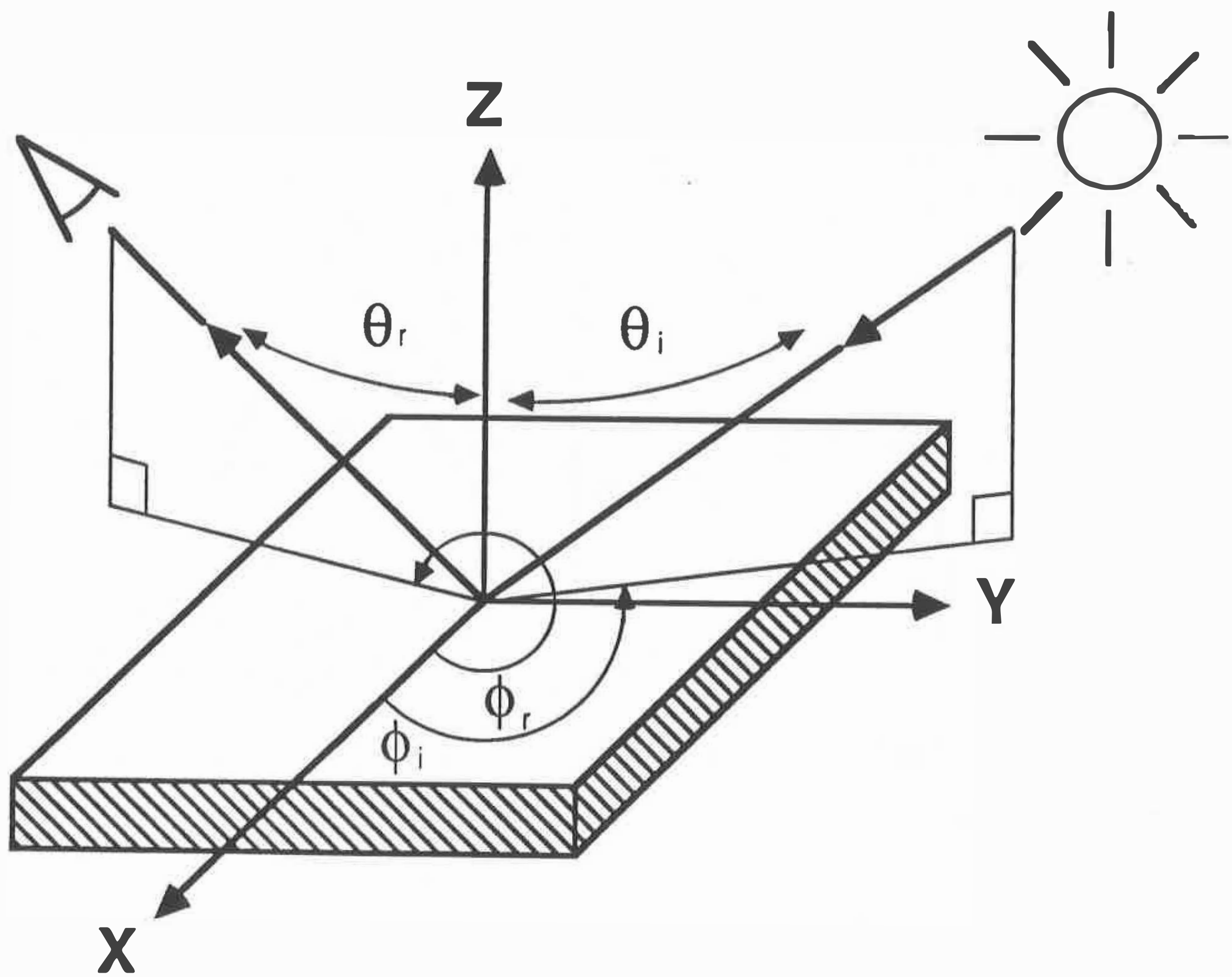

Fig. 2 The local geometry of the incident and the reflected ray can be specified by spherical coordinates (θ_i,ϕ_i) and (θ_r,ϕ_r).

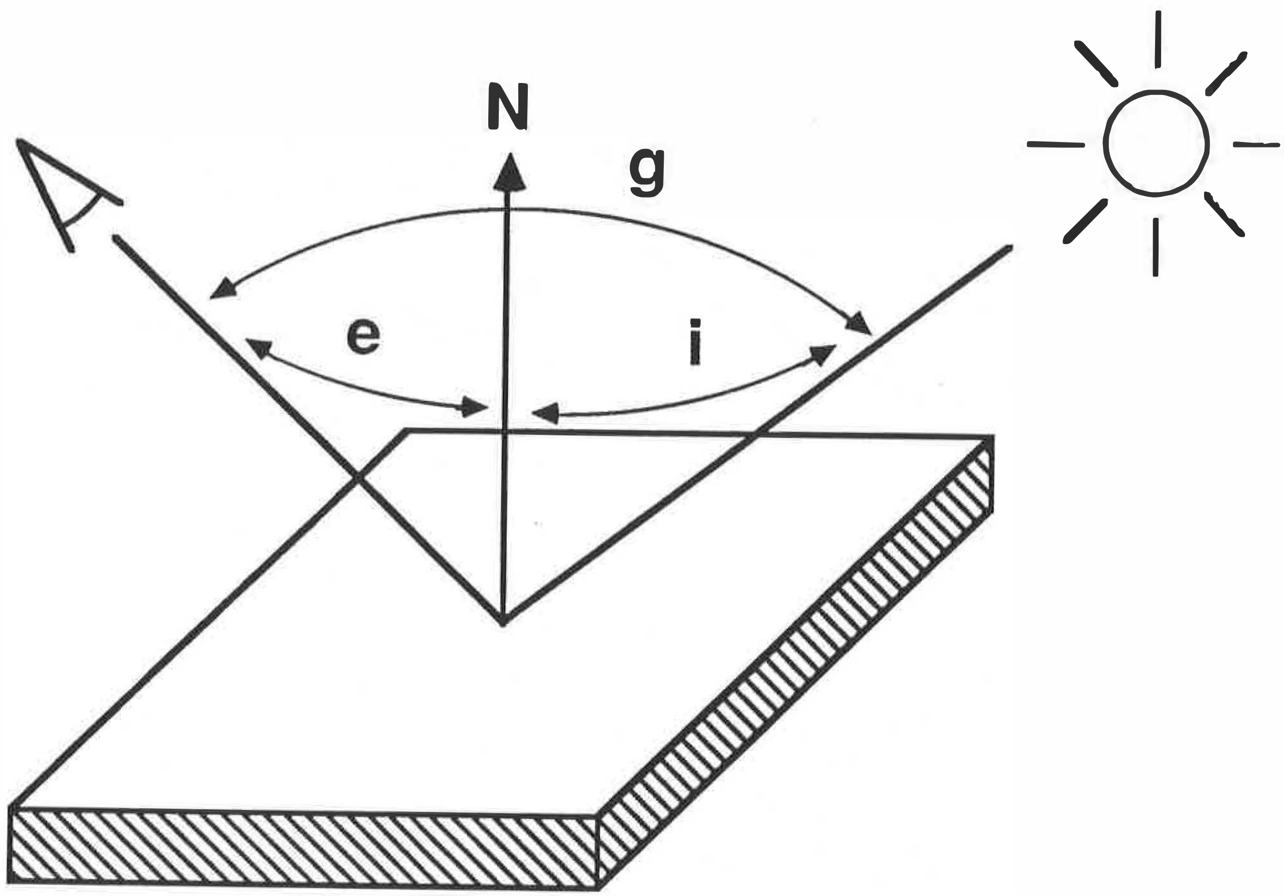

Fig. 3 For isotropic materials, the local geometry of the incident and the reflected ray can be specified by three angles i, e and g. The incident angle i is the angle between the incident ray and the surface normal. The exitant angle e is the angle between the reflected ray and the surface normal. The phase angle g is the angle between the incident and reflected rays.

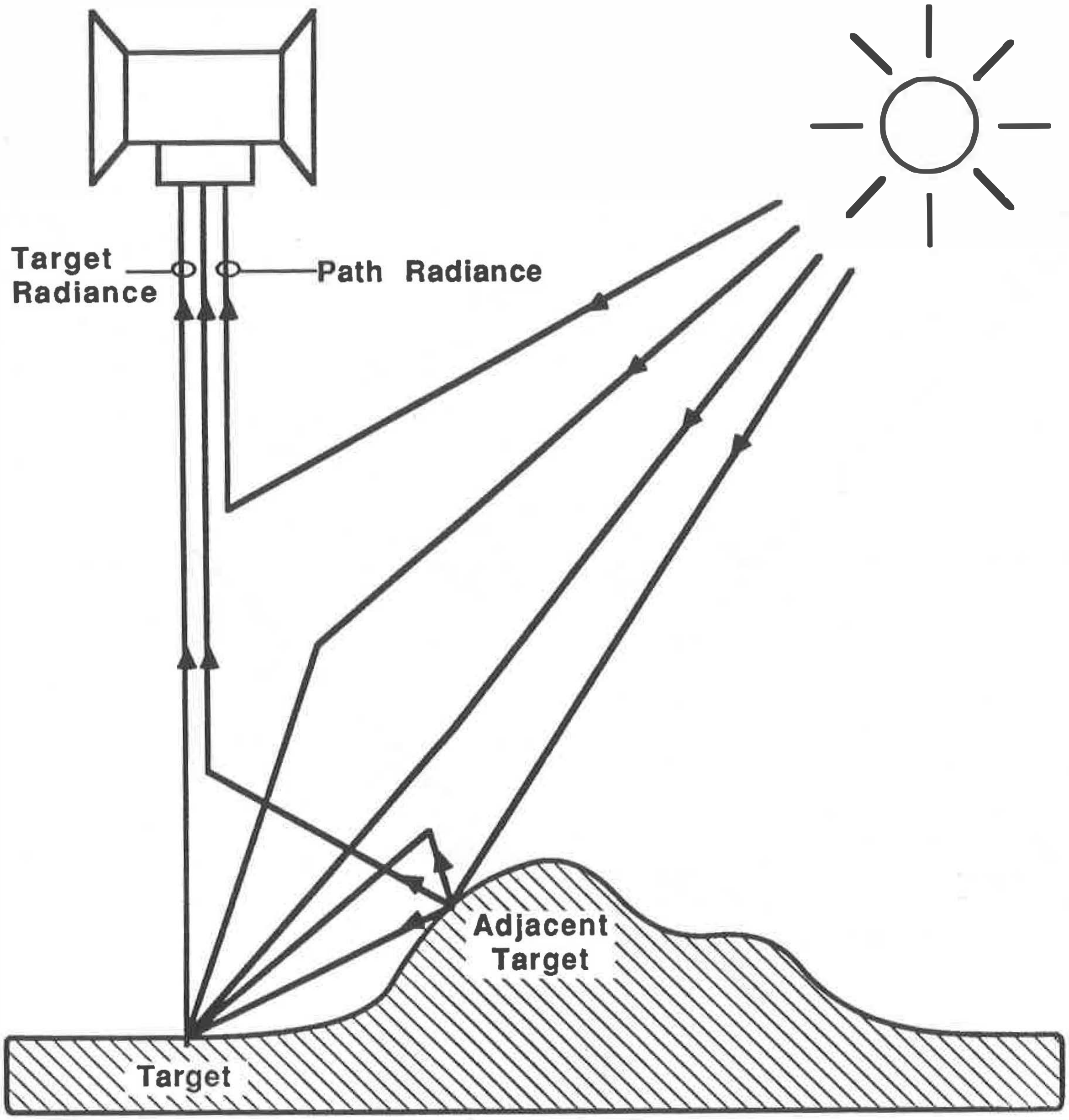

Fig. 4 Components of image irradiance in remote sensing. The target receives direct solar radiation and diffuse sky radiation. Diffuse sky radiation has components due to scattered solar radiation and radiation from adjacent targets that is reflected directly or scattered back to the target. The sensor measures scene radiance reflected from the target with two additional components. Path radiance is radiation scattered to the sensor from the solar beam. Some radiation reflected from adjacent targets also is scattered to the sensor..

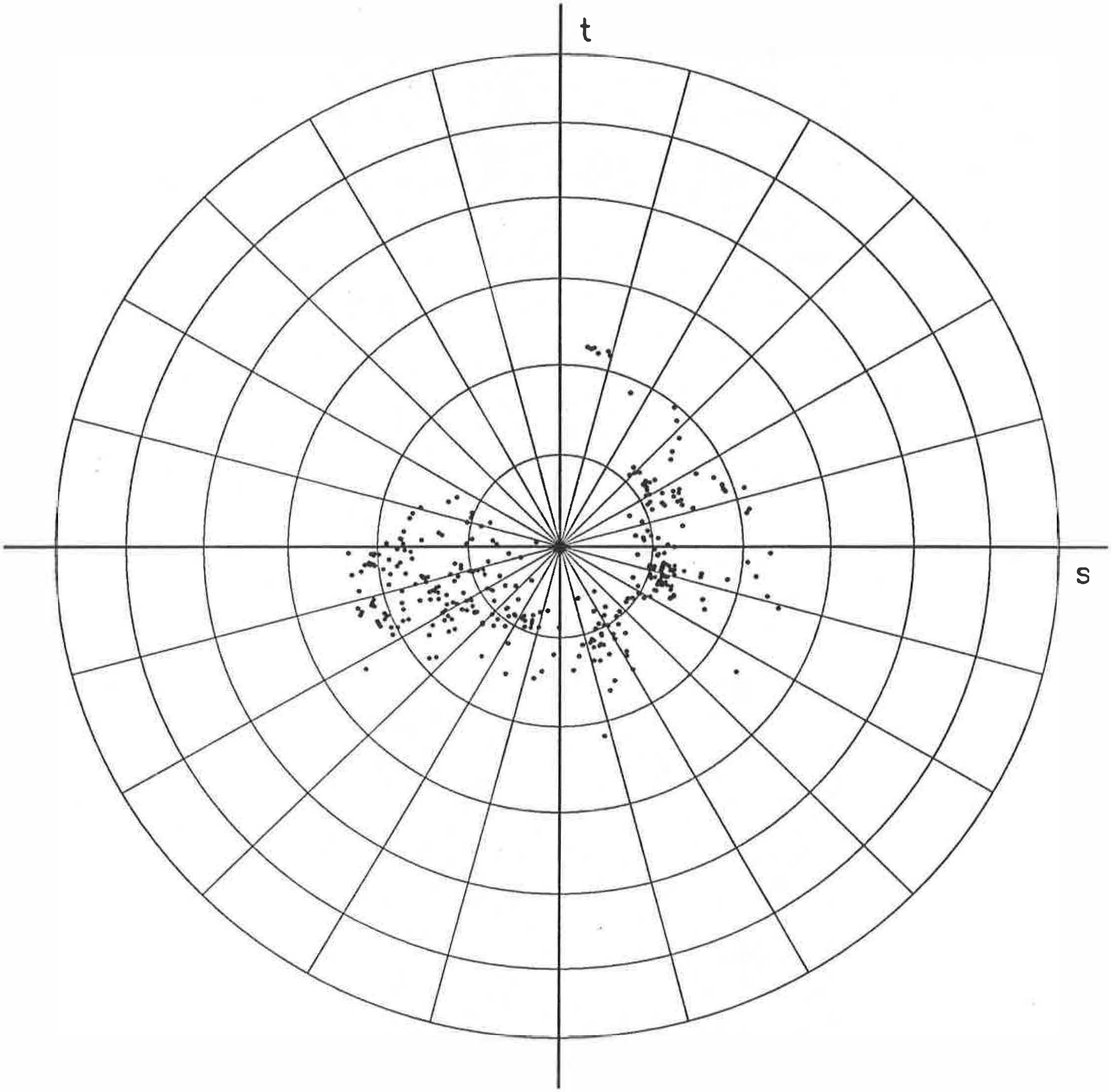

Fig. 5 Slope and aspect of the target set plotted in the azimuthal equal-area projection. Grid lines are in increments of 15° in both slope and aspect. Here, the *s* axis is aligned with east and the *t* axis with north.

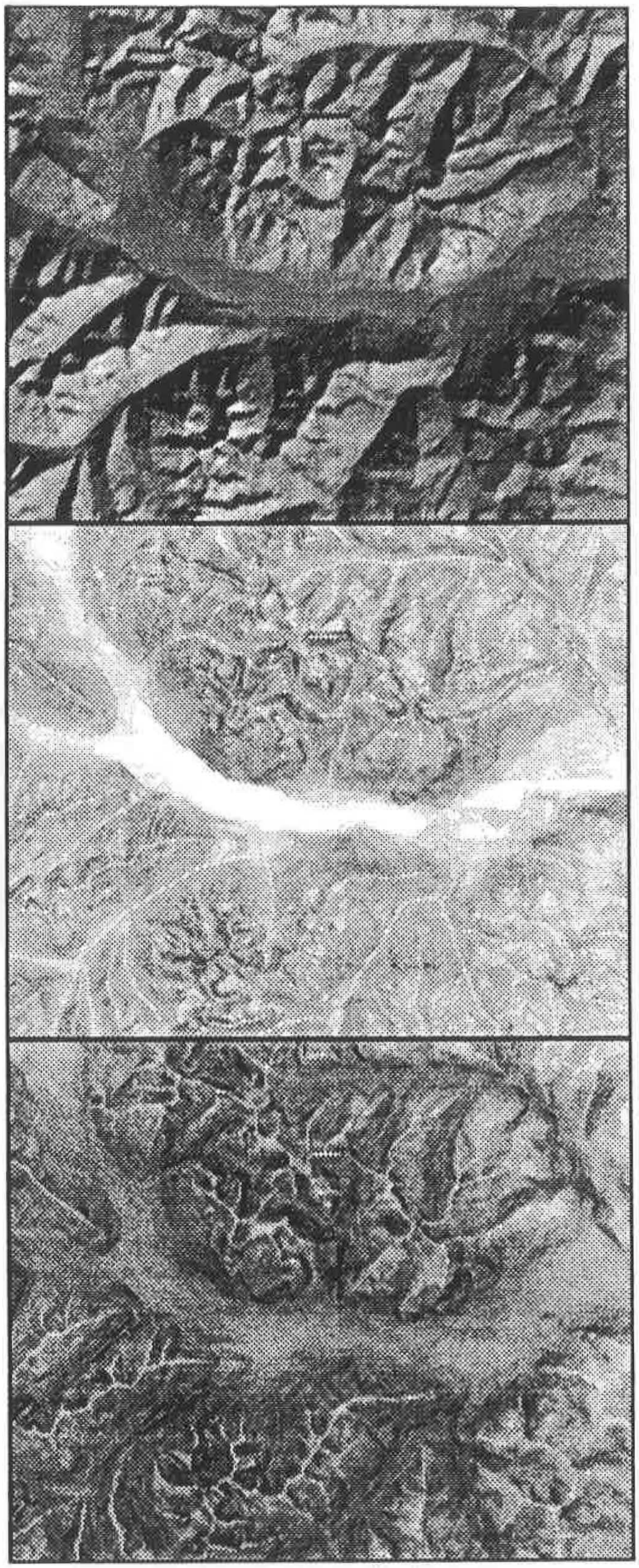

(a)

(b)

(c)

Fig. 6 Synthetic images for St. Mary Lake. Reflectance proportional to $\cos(i)$ is shown in (a) for the sun at an elevation of 38.0 degrees and an azimuth of 145.1 degrees, measured clockwise from north. This corresponds to the position of the sun at 17:52 GMT on September 15, 1981. Reflectance proportional to $(1 + \cos(e))/2$ is shown in (b). The synthetic image for a hemispherical uniform source, including occlusion by adjacent terrain, is shown in (c).

(a)

(b)

Fig. 7 A portion of Landsat MSS image (frame-id 22428-17522), acquired 17:52 GMT on September 15, 1981, is shown in (a). At the time of image acquisition, the sun was at an elevation of 38.0 degrees and an azimuth of 145.1 degrees, measured clockwise from north. The corrected version is shown in (b). Correction is based on the regression equations (23). (The original figure was in colour.)

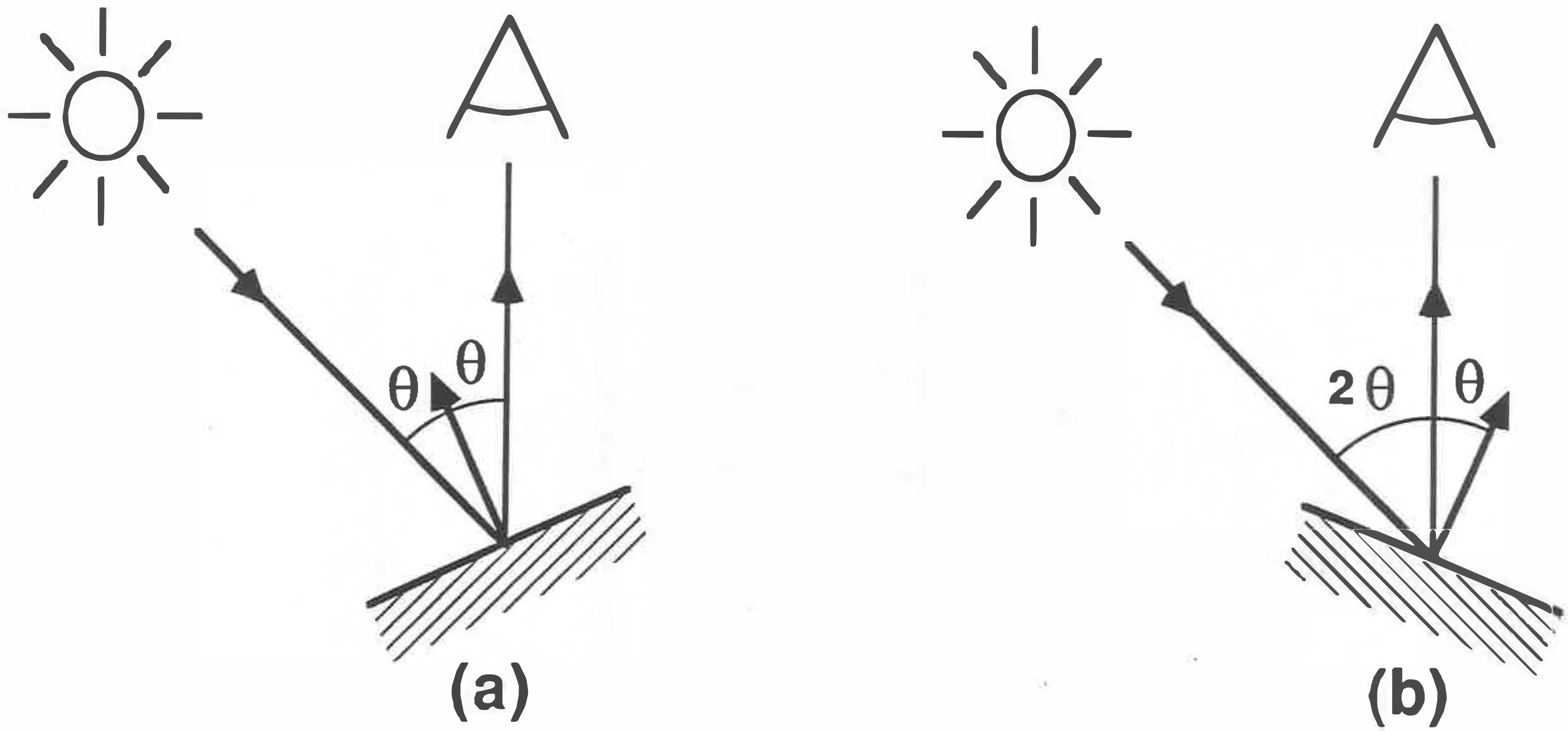

Fig. 8 In (a) the surface is viewed with $i = e = \theta$. In (b) the surface is viewed with $i = 3\theta$ and $e = \theta$. Going from (a) to (b) corresponds to rotating the surface about the fixation point through an angle of 2θ in the plane of the source and viewer.

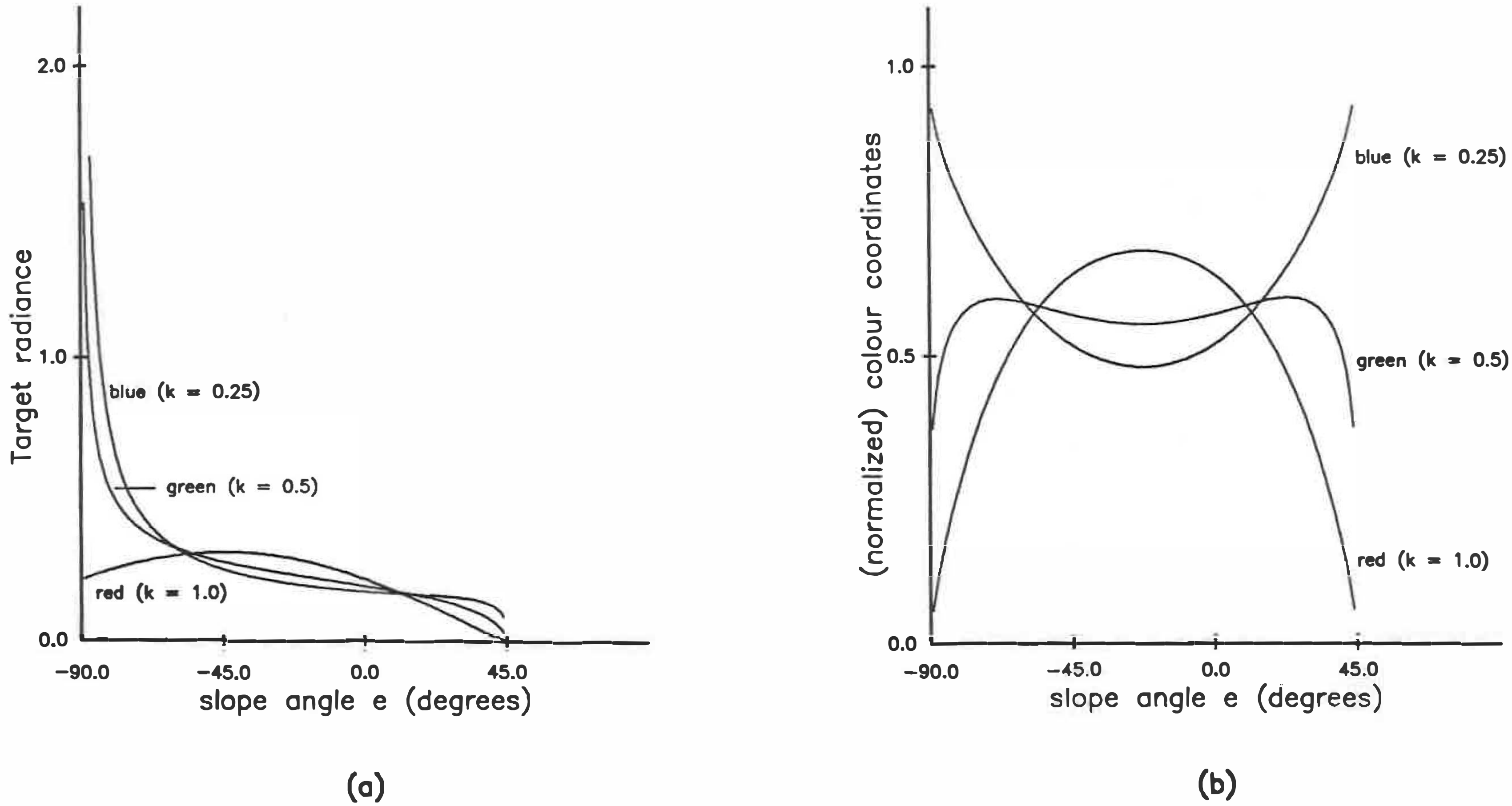

Fig. 9 The direct sun facing slope is at $e = -45$ degrees. In (a) scene radiance is shown for the full range of surface orientations in the plane of the viewer and light source. As e approaches $\pi/2$ in the light source facing direction, scene radiance becomes unbounded for $k = 0.25$ and $k = 0.5$. To emphasize colour shifts, (b) shows scene radiance in normalized colour coordinates. Significant colour shifts occur over the range of orientations for which the surface is visible to the viewer.